Self-Assembling of Er2O3-TiO2 Mixed Oxide Nanoplatelets by a Template-Free Solvothermal Route

ARTICLE *in* CHEMISTRY - A EUROPEAN JOURNAL · OCTOBER 2009

Impact Factor: 5.73 · DOI: 10.1002/chem.200901423 · Source: PubMed

6 AUTHORS, INCLUDING:

Beatriz Julian-Lopez
Universitat Jaume I
47 PUBLICATIONS **2,160** CITATIONS
SEE PROFILE

Jose Antonio Odriozola
Universidad de Sevilla
292 PUBLICATIONS **4,320** CITATIONS
SEE PROFILE

Eloisa Cordoncillo
Universitat Jaume I
106 PUBLICATIONS **1,351** CITATIONS
SEE PROFILE

CHEMISTRY
A EUROPEAN JOURNAL

DOI: 10.1002/chem.200901423

Self-Assembling of Er_2O_3–TiO_2 Mixed Oxide Nanoplatelets by a Template-Free Solvothermal Route

Beatriz Julián-López,[a] Mónica Martos,[a] Natalia Ulldemolins,[a] José A. Odriozola,[b] Eloisa Cordoncillo,[a] and Purificación Escribano*[a]

Abstract: An easy solvothermal route has been developed to synthesize the first mesoporous Er_2O_3–TiO_2 mixed oxide spherical particles composed of crystalline nanoplatelets, with high surface area and narrow pore size distribution. This synthetic strategy allows the preparation of materials at low temperature with interesting textural properties without the use of surfactants, as well as the control of particle size and shape. TEM and Raman analysis confirm the formation of nanocrystalline Er_2O_3–TiO_2 mixed oxide. Mesoscopic ordered porosity is reached through the thermal decomposition of organic moieties during the synthetic process, thus leading to a template-free methodology that can be extended to other nanostructured materials. High specific surface areas (up to 313 $m^2 g^{-1}$) and narrow pore size distributions are achieved in comparison to the micrometric material synthesized by the traditional sol–gel route. This study opens new perspectives in the development, by solvothermal methodologies, of multifunctional materials for advanced applications by improving the classical pyrochlore properties (magnetization, heat capacity, catalysis, conductivity, etc.). In particular, since catalytic reactions take place on the surface of catalysts, the high surface area of these materials makes them promising candidates for catalysts. Furthermore, their spherical morphology makes them appropriate for advanced technologies in, for instance, ceramic inkjet printers.

Keywords: mesoporous materials · nanostructures · rare earths · solvothermal synthesis · titanates

Introduction

Classical areas of application, such as catalysts, passive electronic components, or ceramic materials, are increasing in technical importance with the use of nanoscale oxide particles with a high specific surface area and mean particle diameter between 30 and 300 nm.[1] Hence, one of the most important research areas of the last few decades has been the control of size distribution and shape in the synthesis of particles. Indeed, at the nanometer scale, many materials are known to display very different characteristics and reactivity from those of their bulk counterparts, because the final properties depend not only on the composition but also on the surface properties.[2–4] Furthermore, the combination of attractive properties with a precise porosity is the requirement for new solid materials. Recently, porous materials with defined pore structure and size distribution have been widely applied in many industrial fields, such as separation,[5] adsorption,[6] catalysis,[7] and so on.

In the last few years, a great number of reports have been published related to the synthesis of mesoporous metal oxides. The interest in this kind of material arises from the possibility of combining the intrinsic properties of the unstructured metal oxides with the additional features of a periodic mesoporous solid. It is known that most of the potential applications of the resulting materials (photocatalysis, solar cells, photochromism, sensing, and other applications in nanotechnology) are largely dependent on porosity, total surface area, structural uniformity, and particle size.[8]

Mesoporous materials are usually synthesized with the help of a surfactant as soft template or mesoporous oxides (usually silica) as hard templates.[9] In fact, some authors have reported the synthesis of porous metal oxides without using any template, and obtained relatively low surface area and scattered pore size distribution.[10] Previous reports[11,12]

[a] Dr. B. Julián-López, Dr. M. Martos, N. Ulldemolins, Dr. E. Cordoncillo, Prof. P. Escribano
Department of Inorganic and Organic Chemistry
University Jaume I
Avda. Sos Baynat, s/n, 12071 Castellon (Spain)
Fax: (+34) 964728214
E-mail: escriban@qio.uji.es

[b] Prof. J. A. Odriozola
Department of Inorganic Chemistry, Institute of Materials Science
University of Sevilla-CSIC
Americo Vespucio 49, 41092 Isla de la Cartuja, Sevilla (Spain)

describe a strategy to synthesize microporous and/or mesoporous oxides by controlled thermal decomposition. In this strategy, porosity is generated through thermal decomposition of the precursor and therefore it is based on a different mechanism from the cooperative assembly of the starting molecular species in the common synthesis.

Related to that, Antonietti and co-workers[13,14] have shown a nonclassical pathway (applied gas diffusion technique) for $CaCO_3$ crystallization via colloidal intermediates with mesoscale transformation. They have provided evidence for mesoscale assembly from amorphous primary particles to amorphous aggregates with subsequent crystallization and assembly to $CaCO_3$ mesocrystals, which crystallize in their typical calcite rhombohedral structure. The strategy for the crystalline species to become homogeneous in size and morphology is to add small amounts of polystyrene sulfonate (PSS), because PSS encourages nucleation and decreases the size of the particles.

There is great interest in the synthesis of rare-earth pyrochlore oxides because they are refractory materials with very high melting points, which makes them promising for high-temperature applications. In particular, increasing demand exists for environment-related high-temperature applications, such as catalysts in the control of automobile exhaust gas and combustion gas. But at the same time, high temperatures and important energy costs are required to prepare these refractory materials.

The catalytic activity of the rare-earth pyrochlores is related to their structure. Pyrochlores can be described as a defective fluorite solid solution in which cations are organized in a face-centered-cubic array. To ensure charge neutrality, an eighth of anions are removed, which gives rise to oxygen vacancies that improve the reduction and reoxidation behavior. The rare-earth pyrochlore catalysts should withstand both reducing and oxidizing atmospheres and have high-temperature stability against moisture, high surface area, and uniform particle size distribution. The combination of the intrinsic properties of pyrochlore oxides with those associated with mesoporosity would be interesting for the preparation of highly efficient catalyst supports.[15]

Classical aqueous sol–gel techniques have been widely applied for the synthesis of ternary metal oxides because they offer several advantages over the high-temperature solid-state methods, such as high purity and homogeneity, and low processing temperatures.[16,17] In a previous paper[18] we described the preparation of $Er_2Ti_2O_7$ nanocrystals with a fluorite-like structure by a sol–gel methodology at 700 °C. It was concluded that the structure suffers a gradual atomic rearrangement towards an "ideal" pyrochlore phase when the temperature increases to 800 °C, and shows low surface area properties. However, the aqueous sol–gel chemistry still suffers from some drawbacks resulting from the high reactivity of the metallo-organic precursors towards hydrolysis. On the one hand, the synthesis of ternary and multimetal oxides due to the different reactivities of the individual precursors is particularly difficult in water, and on the other hand, the resulting precipitates contain organic moieties and are often amorphous, which requires further treatment to induce crystallization and often causes a loss of structural order, particle growth, and reduces the surface area.[19,20]

To overcome the sol–gel problems mentioned above and to benefit from the thermal decomposition results, some authors have developed nonaqueous routes using organic solvents to prepare organic–inorganic nanohybrids[21] and crystalline metal oxide nanoparticles.[22–25] According to these investigations, the main advantage of nonaqueous chemistry lies in the possibility of obtaining crystalline products at moderate temperatures. It has been found that, in general, nonaqueous synthesis, in which a solvent is acting as a ligand, provides better control over particle size, shape, crystallinity, and surface properties in comparison to aqueous media chemistry.

In a recent review, Garnweitner and Niederberger[26,27] showed that organic components and organic reaction pathways play a fundamental role in the nonaqueous synthesis of inorganic materials, and that the synthesis of metal oxides not only involves mere nucleation and growth processes, but also the formation of M–O–M bridged bonds, which represents the first step towards building of the solid metal oxide structure. Obviously, in nonaqueous processes the formal oxygen that is required for the formation of the oxygen bridge is provided by the organics used in the synthesis.

Niederberger and Pinna have prepared different mixed metal oxides, such as $BaTiO_3$,[28] $YNbO_4$,[29] and $InSnO_4$[30] among others, by surfactant-free nonaqueous sol–gel routes that are included in a recent minireview.[31] Taking that into account, herein we report a simple solvothermal methodology to prepare mesoporous mixed Er–Ti pyrochlore oxide ($Er_2Ti_2O_7$) spheres with high surface area and a relatively narrow pore size distribution without using templating agents. The mesoporous $Er_2Ti_2O_7$ spherical particles were characterized by X-ray diffraction (XRD), scanning electron microscopy (SEM), transmission electron microscopy (TEM), UV/Vis and laser Raman spectroscopies, and N_2 adsorption/desorption measurements. To the best of our knowledge, this is the first report on the synthesis of porous and nanocrystalline $Er_2Ti_2O_7$ spheres in the absence of templating agents.

Results and Discussion

The thermogravimetric–differential thermal analysis (TG–DTA) of the as-synthesized solvothermal sample (Figure 1) shows two weight losses. The first one, at low temperature, is attributed to the elimination of solvent partially retained in the solid. The second takes place in the temperature range 250–400 °C and corresponds to the combustion of the organic components chemically bound to the as-synthesized material. The simultaneous DTA curve shows, in addition to the exothermic peak associated with this combustion, a second sharp exothermic peak at 800 °C that clearly indicates crystallization of the structure. According to the literature,[32] this peak is attributable to a rearrangement of the

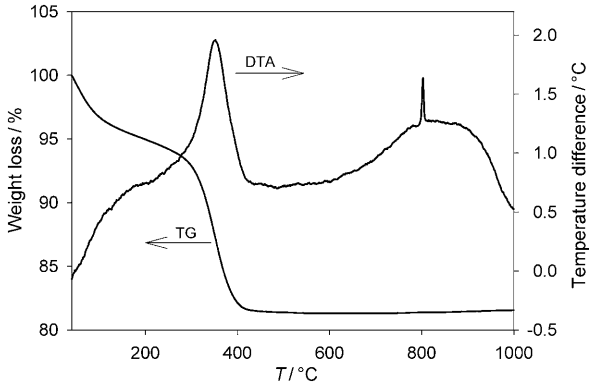

Figure 1. TG–DTA curves of the $Er_2Ti_2O_7$ solvothermal precursor.

oxygen sublattice in the disordered-to-ordered pyrochlore transition found in this type of system.

The morphology and dimensions of the Er–Ti oxide particles were studied by SEM, and images of the samples annealed at 300 and 500 °C are shown in Figure 2. A general view of the materials reveals that the particles exhibit spherical morphology with a wide size distribution ranging from 50 nm to 3 μm. The size distribution changes significantly with temperature. Thus, at 170 °C (not shown), most of the particles are nanometric (50–200 nm) because organic surface modification allows the nanospheres to remain dispersed. Thermal treatment at higher temperatures induces decomposition of organic compounds anchored at the surface, and the nanospheres agglomerate leading to larger particles. Thus, at 300 °C, the large spheres coexist with the initial 50 nm nanoparticles (Figure 2a). Further heating up to 500 °C results in the embedding of small spheres in bigger ones giving rise to microspheres as large as 5 μm (Figure 2b). Interestingly, the spheres exhibit a rough surface, which indicates the existence of an external open porosity. The origin of this bumpy texture will be further discussed.

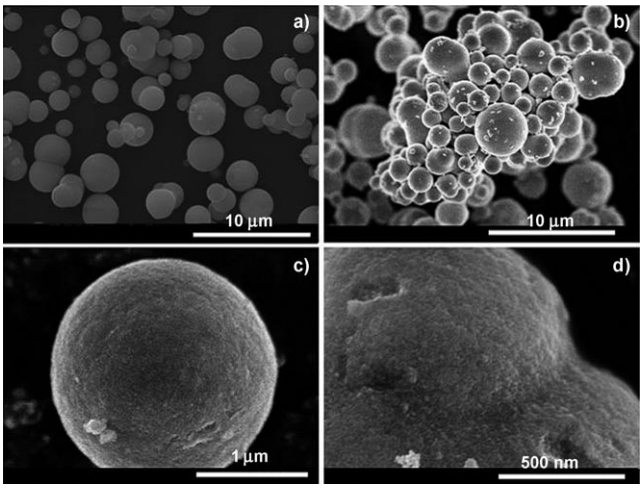

Figure 2. High-resolution SEM images of samples fired at a,c) 300 and b,d) 500 °C.

The development of the $Er_2Ti_2O_7$ pyrochlore phase (JCPDS: 18-0499) was confirmed by XRD at 800 °C. The XRD patterns of samples fired at 300, 500, 700, and 800 °C are presented in Figure 3. At temperatures below 700 °C,

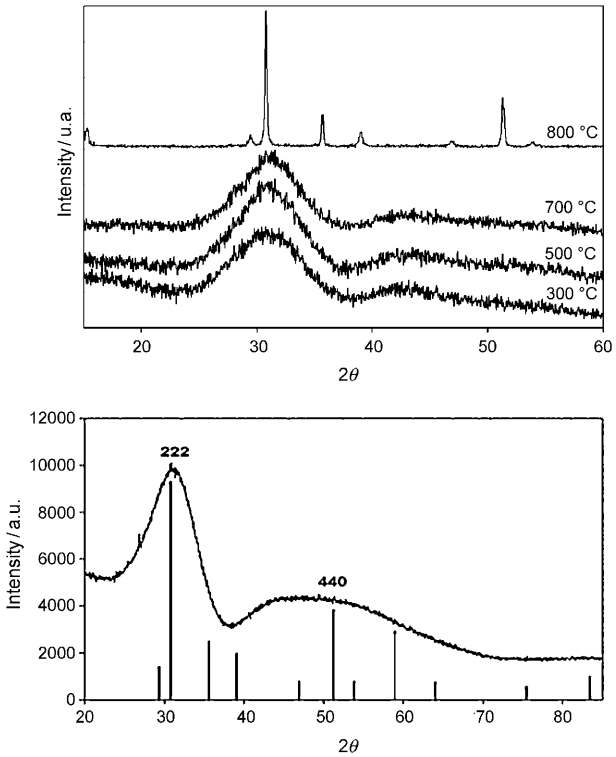

Figure 3. Top) XRD patterns for $Er_2Ti_2O_7$ fired at 300, 500, 700, and 800 °C. Bottom) Accumulated XRD pattern of the sample at 300 °C/2 h. $Er_2Ti_2O_7$ (JCPDS: 18-0499).

the XRD pattern shows a broad diffraction peak centered at around 30° (2θ) that can be attributed to an amorphous material and/or to the presence of very small crystallites. Above this temperature (at 800 °C) a significant change in the XRD pattern is observed; sharp signals indicate that a high level of crystallization has been reached.

To gain insight into the nanocrystallinity at low temperature, more accurate X-ray measurements were performed for the sample fired at 300 °C for 2 h (Figure 3, bottom). This profile indicates that the spheres have a certain long-range order; the position of the peaks is compatible with the even {222} (30.7°) and {440} (51.2°) planes of the pyrochlore structure (JCPDS: 18-0499, space group $Fd\bar{3}m$), which indicates an incipient crystallization of small crystallites at this low temperature.

The featureless XRD patterns of the synthesized materials show a wide peak at approximately $2\theta = 31°$ corresponding to the {222} diffraction planes. If we assume that in the perpendicular direction to this plane the thickness of the nanoparticles is in the order of one to two unit cells, about 2 nm, the full width at half maximum (FWHM) for this peak must be around 5°. Therefore, for these crystalline

domain sizes the XRD pattern must appear like those associated with amorphous materials in which the sizes of domains having long-range order are similar to the size of our nanoparticles, particularly if they are highly textured and expose a surface consisting of {222} planes.

Nevertheless, it should be noted that there is no reference XRD pattern for the fluorite-based Er,Ti oxide, only for $Er_2Ti_2O_7$ pyrochlore. However, the pyrochlore network can be considered as a superstructure of an anion-deficient fluorite atomic arrangement that originated with temperature through a progressive disordering-to-ordering transition. The XRD pattern of our samples showing the even {222} and {440} planes of pyrochlore can also be associated with a defective fluorite structure (for instance, JCPDS 081-1551, $ZrO_{1.87}$ compound).

The average crystallite size of the samples was estimated by using the Scherrer equation from the FWHM of the most intense peak, after correction by the instrumental line broadening. The crystalline domain size, assuming spherical morphology, was estimated to be between 1.3 and 2.0 nm depending on the temperature. Further structural refinements by the Rietveld method were very difficult due to the broadness of the peaks and the reduced crystallinity of the samples.

Only after heating at 800 °C does the XRD pattern of the obtained Er–Ti mixed oxide confirm the crystallization of the pyrochlore structure. Therefore, laser Raman spectroscopy experiments and electron microscopy analyses (SEM and TEM) were carried out to assess the structural arrangement of the synthesized solids. The laser Raman spectra for samples treated at 170 and 500 °C are depicted in Figure 4.

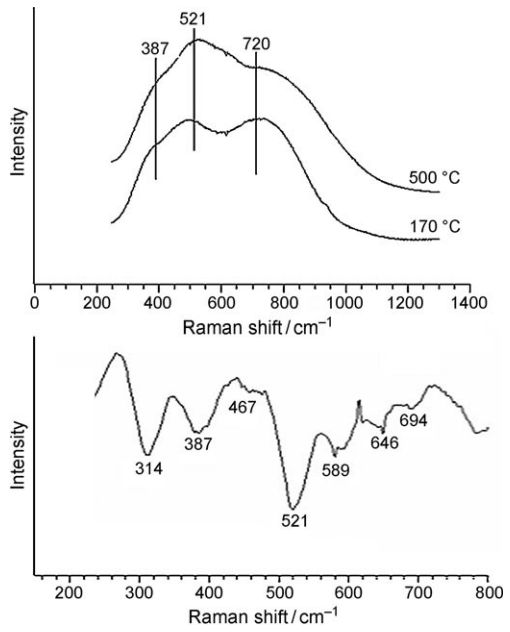

Figure 4. Top) Raman spectra of the obtained Er_2O_3:TiO_2 phases upon heating at 170 and 500 °C. Bottom) Representative second-derivative trace of the Raman spectrum obtained for the sample fired at 500 °C.

According to group theory, the Raman spectrum of a pyrochlore structure has six active Raman modes corresponding to the following irreducible representation: $A_{1g}+E_g+4F_{2g}$. Site symmetry of the A and B cations in the structure (*D*3*d*) results in nonactive Raman modes and hence the active Raman modes involve just the motion of the oxygen atoms in the pyrochlore structure.[33] This fact contributes to the almost insensitive nature of the Raman spectra to cation substitution in either the A or B sites, although slight shifts of the vibrational frequencies are observed. Furthermore, the bands broaden and the peak intensities decrease.[34] Literature data show that the Raman spectra of crystalline $Ln_2Ti_2O_7$ pyrochlores are dominated by two intense bands at about 310 and 510 cm^{-1} arising from the O-A-O (E_g+F_{2g}) bending and A–O (A_{1g}) stretching modes, respectively. The two modes of the first peak may be resolved as a shoulder at 330 cm^{-1} (E_g mode) of a main peak at 310 cm^{-1} (F_{2g} mode).[35]

The spectra of the samples fired at 170 and 500 °C (Figure 4, top) present several broad bands overlapped from 300 to 800 cm^{-1}, which point to the existence of a not well-ordered solid at both temperatures. The characteristic Raman band corresponding to the ideal crystalline pyrochlore structure at around 310 cm^{-1} cannot be clearly detected in these overlapped signals, but it is confirmed by analyzing the second derivative of the registered spectra (Figure 4, bottom). The main absorption band at 521 cm^{-1} indicates the existence of a certain pyrochlore order in our materials. According to the literature,[36,37] this absorption band may not be ascribed to either Er_2O_3 or TiO_2 rutile or anatase.

The last absorption band exhibits higher intensity and a 15 cm^{-1} redshift after firing at 500 °C. This redshift behavior may be indicative of oxygen deficiency, as already reported for TiO_2 oxygen-deficient phases.[38] Furthermore, a new contribution at around 600 nm is also detected at 500 °C. A recent publication concerning Zr-Ce-Pr-O materials[39] ascribed two Raman bands at 464 and 560 cm^{-1} to a fluorite-type structure and to the presence of oxygen vacancies, respectively. This behavior is in agreement with our systems, in which the thermal treatment involves a redshift and the appearance of a new contribution. Therefore, Raman data reveal an increase of the oxygen defects in the structure with temperature, which is in agreement with a progressive transformation of the material from a defective fluorite structure to the pyrochlore network.

Figure 5 shows a set of TEM images and selected-area electron diffraction (SAED) patterns of the erbium–titanium oxide samples. Figure 5a presents a general view of the material, which illustrates the spherical morphology. Even if the particle size distribution is not very narrow, an important number of sub-micrometer particles are still present after 500 °C. As clearly illustrated in Figure 5c and d (high-resolution TEM (HRTEM) images), the microspheres are formed by self-assembled thin nanoparticles. The almost 2D morphology of the nanoparticles is also confirmed by SEM (Figure 2).

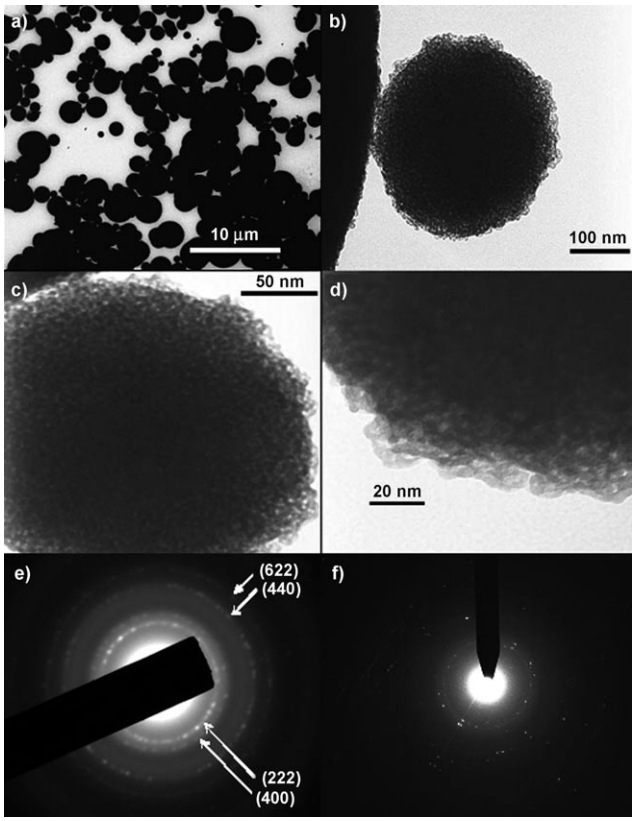

Figure 5. TEM images of the synthesized samples. a–d) High-resolution images of the sample fired at 500 °C. On increasing the resolution the presence of self-assembled nanoplatelets giving rise to a mesoporous structure is clearly seen. e, f) SAED of nanoplatelets corresponding to the samples fired at 170 and 300 °C, respectively. The planes are assigned according to Zhang et al.[40]

Although it was not possible to provide the exact dimensions of the nanoparticles, different measurements at the edges of the spheres allow us to propose an elongated morphology with aspect ratio close to 2 and long axis ranging between 5 and 10 nm that leave void spaces within them, thus resulting in a homogeneous vesicle-like porous structure. The existence of the small nanoparticles and the porosity were already suggested from the bumpy texture of the microsphere surface in the high-resolution SEM images, which is now confirmed. Figure 6 shows a high-resolution SEM image in which this structure is clearly seen.

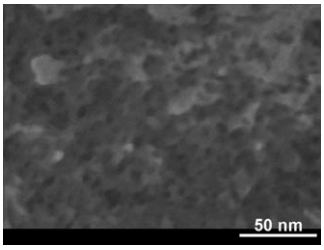

Figure 6. High-resolution SEM image of $Er_2Ti_2O_7$ fired at 500 °C.

Homogeneous pores are randomly distributed within the whole spherical material, and the particle size remains almost constant with the calcination temperature, in accordance with the XRD results. Only a slight increase in the average pore size (from 1 to 3 nm) can be detected by HRTEM images as a consequence of particle rearrangement with temperature.

SAED images for samples fired at 170 and 300 °C are presented in Figures 5e and f. In both cases a spotted-ring pattern showing a wide distribution of distances centered at 0.290, 0.250, 0.180, and 0.150 nm is evident, in close agreement with the even *hkl* planes of the pyrochlore structure. The former interplanar distances can also be assigned to the Er_2O_3 structure. The {222} planes of both the $Er_2Ti_2O_7$ pyrochlore and Er_2O_3 structures show similar atom distribution and geometry but the lattice parameters are slightly bigger in the case of the erbium oxide. The nanoparticle size and morphology, nanoplatelets with about one unit cell thickness, account for the stacking of just a few planes of the pyrochlore structure in the [111] direction. Surface reconstruction for minimizing the surface energy may result in a rippled surface containing erbium and oxygen atoms, which account for the diffraction ring observed in Figure 5 f.

Elemental analysis using both transmission and scanning microscopes, performed by energy-dispersive X-ray (EDX) analysis for samples fired at all temperatures, confirmed the homogeneous distribution of the heavy elements (Er and Ti) in the analyzed regions, and also that the composition was very close to the $Er_2Ti_2O_7$ stoichiometry.

Small-angle X-ray scattering (SAXS) was used to explore the microstructure on the nanometer scale. The XRD patterns obtained for the particles heated at 170 (as-synthesized), 300, and 500 °C are depicted in Figure 7. A broad peak centered at around $2\theta = 1.8°$ can be seen in the pattern of the as-synthesized sample, which indicates a mesoscopic order regularity. This peak becomes narrower and more intense on firing at higher temperatures. The feature is accompanied by a shift towards lower 2θ values, appearing at $2\theta = 1.5°$ after firing at 500 °C. This diffraction line corresponds

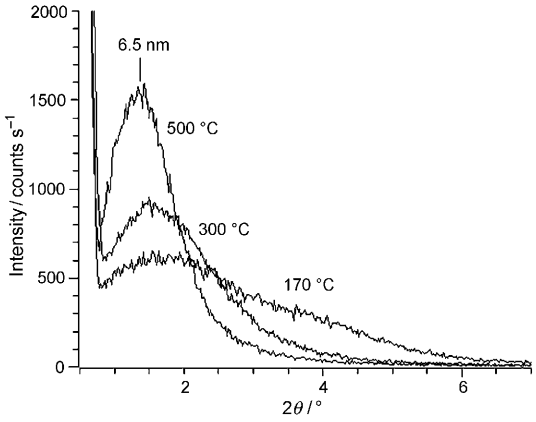

Figure 7. SAXS patterns of the Er,Ti fluorite oxide material fired at 170, 300, and 500 °C.

to a correlation distance between the pores of 6.5 nm. The increase in the correlation distance (counting nanoparticle plus pore space) is in good agreement with the XRD results and HRTEM observations.

N_2 adsorption–desorption isotherms and Barrett–Joyner–Halenda (BJH) desorption pore size distribution plots of the material fired at different temperatures are shown in Figure 8. The sample fired at 500 °C presents reversible

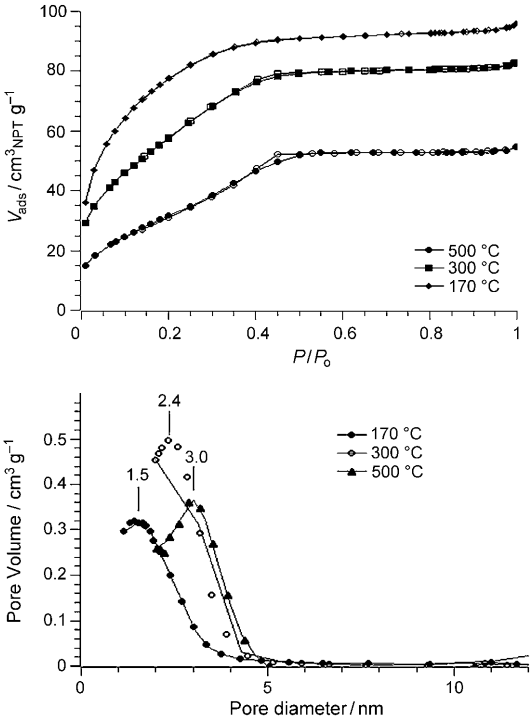

Figure 8. Top) Nitrogen adsorption–desorption isotherms of samples fired at the indicated temperatures and bottom) pore size distributions.

type IV adsorption–desorption isotherms with an H2-type hysteresis loop indicative of mesoporosity. The samples fired at 170 and 300 °C might be classified as type I. The type I isotherms are reversible and characteristic of solids having small pore radius and relatively small external surfaces. On the other hand, a feature common to many hysteresis loops is that the steep region of the desorption branch leading to the lower closure point occurs (for a given adsorptive at a given temperature) at a relative pressure that is almost independent of the nature of the porous adsorbent but depends mainly on the nature of the adsorptive (e.g., for nitrogen at its boiling point at $p/p° = 0.42$, which according to the Kelvin equation corresponds to a pore radius of ca. 3 nm). In our case, except for the sample calcined at 500 °C that presents a very small hysteresis loop, the pore size distribution shows a maximum between 1.5 and 3 nm. This, as described by Singh et al.,[41] can be classified as micropores (pores with widths not exceeding about 2 nm) or mesopores by taking into account that this limit is to some extent arbitrary, since the pore-filling mechanisms are dependent on the pore shape and are influenced by the properties of the adsorptive and by the adsorbent–adsorbate interactions. Table 1 gives information about textural properties considering that the observed pores fall in the mesoporosity range.

Table 1. Specific surface area (S_{BET}) and pore size distribution calculated from the desorption branch of the isotherm with the BJH method, and total pore volume of the solvothermal samples fired at different temperatures.

T [°C]	S [$m^2 g^{-1}$]	Total pore volume [$cm^3 g^{-1}$]	Pore size [nm]
170	313	0.17	1.5
300	218	0.13	2.4
500	141	0.10	3.0

The high value of the specific surface area for the sample fired at 170 °C (S_{BET} up to 313 $m^2 g^{-1}$), in spite of the fact that this sample still contains organic matter, can be accounted for by the small size of the nanoparticles and the number of void spaces between the nanoparticles inside the microspheres, as detected by XRD and HRTEM techniques. An increase in the firing temperature results in a diminution of the BET surface area, as a consequence of sintering processes. However, high values are still obtained at elevated temperatures, for instance, 45 $m^2 g^{-1}$ has been measured after heat treatment of the sample at 700 °C.

Because the catalytic reactions take place on the surface of catalysts, the reaction rates are greatly related to the surface area of the catalysts. Therefore, in an attempt to enhance the textural properties, especially the specific surface area, some experiments incorporating several surfactants of different nature (cationic cetyltrimethylammonium bromide (CTAB) and nonionic P123 templates) were performed, but the surface area remained almost constant. It seems that the porosity generated in situ during the solvothermal synthesis by decomposition of organic moieties is important enough to consider as negligible the incorporation of additional structure-directing agents.

The pore size distribution was obtained from these isotherms by using the BJH method[42] (Figure 8 , bottom). A sharp pore size distribution is observed with a maximum that shifts from 1.5 nm for the as-synthesized samples to 3.0 nm for the sample fired at 500 °C. The average pore sizes are completely in agreement with SAXS and HRTEM results.

Considering the above-mentioned XRD and TEM results and those previously reported,[26,27,31] a nanometric mixed oxide was prepared by a nonaqueous process, in which the formal oxygen required is provided by the organics used in the synthesis. A proposed mechanism that may account for the mixed metal oxide morphology is shown in Scheme 1. First, with the addition of acetylacetone (Hacac) to the erbium acetate ethanolic solution an acetylacetonate erbium complex is formed. In the presence of the acetate counterions of the erbium species, the possible formation of an ester between the employed carboxylic acid and ethanol may result in the formation of molecular erbium oxo-aggre-

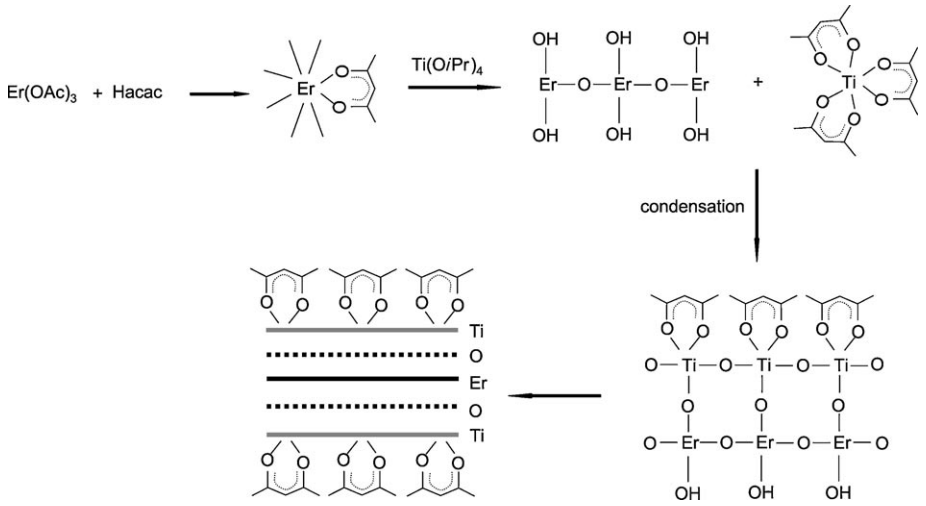

Scheme 1. Proposed mechanism for the formation of Er_2O_3–TiO_2 mixed oxide nanoplatelets.

gates, since the generated water would give rise to partial hydrolysis of the erbium complex.[31,43,44] These clusters would contain acac, hydroxyl, acetate, and/or alkoxy ligands as well as Er−O−Er bonds. Although these clusters have not been previously described for erbium species, similar structures have been proposed for yttrium complexes[45] and yttrium complexes resulting in the formation of TiY mixed oxides.[46] The addition of the titanium precursor promotes the destabilization of the Er–acetylacetonate complex because of its higher affinity to β-diketonate ligands, together with the substoichiometric amount of ligands that is not enough to coordinate both ions. The formation of a heterometal dinuclear 3d–4f assembled molecular system between Cr^{III} and Er^{III} species[47] or Ti^{IV} and Y^{III} species has been previously reported[48] or more recently, by using solvothermal methods, the synthesis of $YNbO_4$[29] in which the alcoholysis of acac−M bonds is a key step in the mixed oxide synthesis. The OH groups located at the surface of this erbium oxide cluster undergo condensation with titanium complexes, which leads to a Ti-O-Er-O-Ti sequence similar to that of the {222} pyrochlore plane (Scheme 1). The growth of the crystalline structure is then limited by grafting of the acac groups at the Ti surface. This mechanism can explain the morphology observed in TEM images and the preferred {222}-plane orientation in the X-ray patterns.

The above nanoplatelets aggregate during the solvothermal process in such a way that the surface energy is minimized, that is, the spherical morphology as shown in Figure 9.

The generation of the mesoporosity in these materials may result from the use of the acac ligand and metallo-organic precursors ($Ti(OiPr)_4$) in the ethanolic medium. From the TG data, the existence of organic compounds chemically bound to the oxide particles after the synthesis process (at 170 °C) can be established. Considering the high stability of the coordination compounds between metals and acac groups,[49] a hydrophobic surface can be derived from the presence of acac species on the nanoparticle surface, that is, the acetylacetone molecule acts as an organic templating agent during the hydrolysis/polycondensation steps.

Previous investigations on this system synthesized by the sol–gel methodology[18] did not achieve such special features as those obtained by the solvothermal route. For instance, sol–gel products required firing steps at high temperatures (>700 °C) to obtain crystallization, and the particles did not show any specific morphology which did not contribute to generating a high surface area. Indeed, the specific surface of sol–gel $Er_2Ti_2O_7$ after firing at 700 °C is 7.40 $m^2 g^{-1}$. The comparison of these data with those reported herein underlines the difficulty in achieving a tailored porosity by the sol–gel process. We think that the solvothermal route opens up a new research field to prepare highly porous materials with enhanced applications in catalysis.

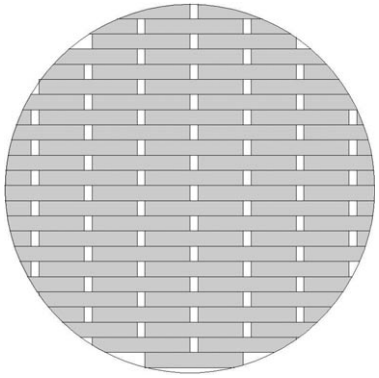

Figure 9. Schematic representation of the Er_2O_3–TiO_2 nanoplatelet distribution on the spherical particle.

Conclusion

A simple template-free strategy has been developed for the synthesis of mesoporous and nanocrystalline mixed oxide particles. Herein, the synthesis of erbium titanate microspheres by a solvothermal route is reported for the first time. The methodology proposed allows the preparation of materials at low temperature with excellent textural properties without the use of surfactants. The control of the particle size and shape can be modulated by the synthesis conditions. TEM and Raman analysis confirm the formation of an incipient pyrochlore structure at low temperatures (170 °C). Mesoscopic ordered porosity is reached through the thermal

decomposition of organic moieties during the synthetic process. High specific surface areas (up to $313\,m^2g^{-1}$) and narrow pore size distribution (at around 2.0 nm) are achieved in comparison to the micrometric material synthesized by the traditional sol–gel route. This study opens new perspectives for the development, by solvothermal methodologies, of porous and nanocrystalline mixed metal oxides for advanced applications, which combines these features with the classical properties of the oxides (catalyst, magnetization, heat capacity, conductivity, etc. in the case of pyrochlores).

Experimental Section

Preparation of $Er_2Ti_2O_7$: $Er_2Ti_2O_7$ material was synthesized by a solvothermal methodology with tetraisopropyl orthotitanate ($Ti(OiPr)_4$, Strem, 98%) and erbium acetate ($Er(OAc)_3$, Strem, 99.9%) as precursors, absolute ethanol (Scharlau, 99.9%) as solvent, and acetylacetone (Hacac, Panreac, analysis grade) as chelating ligand to dissolve the erbium precursor. The corresponding amount of the erbium precursor to prepare 1 g of $Er_2Ti_2O_7$ was dissolved in an Hacac ethanolic solution under reflux at 70 °C. The Er/acac ratio was 1:4 in absolute ethanol (50 mL). Once the erbium precursor was dissolved, Ti isopropoxide was added and the solution was stirred for 30 min. The final mixture was transferred into a stainless steel autoclave with Teflon cups of 125 mL capacity (Parr acid digestion bombs) and subsequently heated at 170 °C for 24 h. After cooling to room temperature naturally, the resulting suspension was centrifuged, thoroughly washed with acetone repeatedly to remove inorganic and organic residues, and dried in air at room temperature to yield a pink powder. The as-synthesized powders were fired at different temperatures (300, 500, 700 °C) during 2 h with a heating rate of $5\,°C\,min^{-1}$.

Characterization: DTA and TG analysis were performed in a Mettler Toledo model SDTA 851e. All experiments were run in a 150 μL Pt crucible from 25 to 1200 °C with a heating rate of $10\,°C\,min^{-1}$ and under an air atmosphere. Phase analysis of the fired samples was performed by powder XRD with a Siemens D5000 diffractometer with $Cu_{K\alpha}$ radiation. Data were collected by step-scanning from $2\theta = 20$ to 70° with a step size of 0.05°, 10 s of counting time at each step, and accumulating over two XRD cycles. The goniometer was controlled by the "Siemens DIFFRACT Plus" software, which also determined diffraction peak positions and intensities. The instrument was calibrated with an external Si standard. SAXS analysis was performed with a Philips X'Pert diffractometer using CuK_α radiation ($\lambda = 0.15418$ nm). The diffractometer was operated at 40 kV and 40 mA. SAXS measurements were carried out with a step size of 0.002°, a 20 s exposure time, and a position-sensitive detector (PSD) length of 0.5170 (2θ). High-resolution SEM images were taken in a Hitachi S5200 instrument. The in-lens sample holder allowed a resolution of 0.5 nm. In all the experiments, uncoated samples were analyzed at an acceleration voltage of 5 kV with a secondary electron detector. The composition of the samples was obtained by EDX analysis, conducted with an EDX spectrometer (Oxford Instruments) coupled to a Leica scanning electron microscope, model Leo 440. TEM observations were carried out in a Philips CM200 microscope operating at 200 kV. The samples were dispersed in ethanol by sonication and dropped on a copper grid coated with a carbon film. SAED images were taken with a camera length of 1.35 m. N_2 adsorption–desorption isotherms were collected on a Micromeritics ASAP2020 gas adsorption analyzer at 77 K, after degassing the samples at 398 K overnight on a vacuum line. The surface areas were calculated by the BET method and the pore size distributions were calculated from the desorption branch of the isotherm by the BJH method. Laser Raman spectra were obtained with a Horiba Jobin Yvon HR800 UV spectrometer with a 514.5 nm excitation line and a $600\,g\,mm^{-1}$ grating. All the spectra were taken with a 1 s exposure time, five scans, and a pinhole of 100 mm.

Acknowledgements

This research was supported by the Spanish Government (MAT-2008–03479) and Bancaixa Foundation–Universitat Jaume I (P1 1B2007–47) projects. M.M. and B.J.-L. especially thank UJI and MEC for their PhD fellowship and "Ramon y Cajal" contract, respectively.

[1] S. Feldmann, H. O. Jungk, *Angew. Chem.* **2001**, *113*, 372; *Angew. Chem. Int. Ed.* **2001**, *40*, 359.
[2] J. J. Li, L. Zou, D. Hartono, C. N. Ong, B. H. Bay, L. Y. L. Yung, *Adv. Mater.* **2008**, *20*, 138.
[3] A. P. Alivisatos, *J. Phys. Chem.* **1996**, *100*, 13226.
[4] C. Burda, X. Chen, R. Narayanan, M. A. El-Sayed, *Chem. Rev.* **2005**, *105*, 1025.
[5] T. Sen, A. Sebastianelli, L. J. Bruce, *J. Am. Chem. Soc.* **2006**, *128*, 7130.
[6] L. Mercier, T. Pinnavaia, *Adv. Mater.* **1997**, *9*, 500.
[7] D. E. De Vos, M. Dams, B. F. Sels, P. A. Jacobs, *Chem. Rev.* **2002**, *102*, 3615.
[8] S. Förster, M. Antonietti, *Adv. Mater.* **1998**, *10*, 195.
[9] C. T. Kresge, M. E. Leonowicz, W. J. Roth, J. C. Vartuli, J. S. Beck, *Nature* **1992**, *359*, 710.
[10] A. Durairajan, H. C. Mercado, B. Haran, R. White, B. Popov, *J. Power Sources* **2002**, *104*, 157.
[11] C. Yu, L. Zhang, J. Shi, J. Zhao, J. Gao, D. Yan, *Adv. Funct. Mater.* **2008**, *18*, 1544.
[12] J. D. Bass, C. Boissiere, L. Nicole, D. Grosso, C. Sanchez, *Chem. Mater.* **2008**, *20*, 5550.
[13] T. Wang, H. Cölfen, M. Antonietti, *J. Am. Chem. Soc.* **2005**, *127*, 3246.
[14] A. W. Xu, M. Antonietti, H. Cölfen, F. Yue-Ping, *Adv. Funct. Mater.* **2006**, *16*, 903.
[15] A. G. Stepanov, M. V. Luzgin, S. S. Arzumanov, W. Wang, M. Hunger, D. Freude, *Catal. Lett.* **2005**, *101*, 181.
[16] L. Kurihara, S. L. Suib, *Chem. Mater.* **1994**, *6*, 609.
[17] Y. B. Mao, T. J. Park, S. Wong, *Chem. Commun.* **2005**, 5721.
[18] M. Martos, B. Julián-López, E. Cordoncillo, P. Escribano, *J. Phys. Chem. B* **2008**, *112*, 2319.
[19] C. C. Wang, J. Y. Ying, *Chem. Mater.* **1999**, *11*, 3113.
[20] E. A. Barringer, H. K. Bowen, *J. Am. Ceram. Soc.* **1982**, *65*, c-199.
[21] N. Pinna, *J. Mater. Chem.* **2007**, *17*, 2769.
[22] I. Djerdj, D. Arcon, Z. Jaglicic, M. Niederberger, *J. Phys. Chem. C* **2007**, *111*, 3614.
[23] M. Niederberger, G. Garuweitner, N. Pinna, G. Neri, *Prog. Solid State Chem.* **2005**, *33*, 59.
[24] J. Ba, A. Feldhoff, D. F. Rohlfing, M. Wark, M. Antonietti, M. Niederberger, *Small* **2007**, *3*, 310.
[25] M. Niederberger, N. Pinna, J. Polleux, M. Antonietti, *Angew. Chem.* **2004**, *116*, 2320; *Angew. Chem. Int. Ed.* **2004**, *43*, 2270.
[26] G. Garnweitner, M. Niederberger, *J. Mater. Chem.* **2008**, *18*, 1171.
[27] M. Niederberger, G. Garnweitner, *Chem. Eur. J.* **2006**, *12*, 7282.
[28] M. Niederberger, *J. Am. Chem. Soc.* **2004**, *126*, 9120.
[29] M. Niederberger, *Chem. Asian J.* **2008**, *3*, 746.
[30] M. Niederberger, *Chem. Mater.* **2006**, *18*, 2848.
[31] N. Pinna, N. Niederberger, *Angew. Chem.* **2008**, *120*, 5372; *Angew. Chem. Int. Ed.* **2008**, *47*, 5292.
[32] A. V. Shlyakhtina, J. C. C. Abrantes, L. L. Larina, L. G. Scherbakova, *Solid State Ionics* **2005**, *176*, 1653.
[33] M. Maczka, J. Hanuza, K. Hermanowicz, A. F. Fuentes, K. Matsuhira, Z. Hiroi, *J. Raman Spectrosc.* **2008**, *39*, 537.
[34] M. Glerup, O. F. Nielsen, F. W. Poulsen, *J. Solid State Chem.* **2001**, *160*, 25.
[35] F. W. Poulsen, M. Glerup, P. Holtappels, *Solid State Ionics* **2000**, *135*, 595.
[36] J. B. Gruber, R. D. Chirico, E. F. Westrum, Jr., *J. Chem. Phys.* **1982**, *76*, 4600.
[37] Y. L. Li, T. Ishigaki, *J. Phys. Chem. B* **2004**, *108*, 15536.
[38] J. C. Parker, R. W. Siegel, *J. Mater. Res.* **1990**, *5*, 1246.

[39] J. Mikulova, S. Rossignol, F. Gérard, D. Mesnard, C. Kappenstein, D. Duprez, *J. Solid State Chem.* **2006**, *179*, 2511.
[40] A. Zhang, M. Lü, Z. Yang, G. Zhou, Y. Zhou, *Solid State Sci.* **2008**, *10*, 74.
[41] K. S. W. Sing, D. H. Everett, R. A. W. Haul, L. Moscou, R. A. Pierotti J. Rouquerol, T. Siemieniewska, *Pure Appl. Chem.* **1985**, *57*, 603.
[42] E. P. Barrett, L. G. Joyner, P. P. Halenda, *J. Am. Chem. Soc.* **1951**, *73*, 373.
[43] U. Schubert, *Acc. Chem. Res.* **2007**, *40* , 730.
[44] L. Rozes, N. Steunou, G. Fornasieri, C. Sanchez, *Monatsh. Chem.* **2006**, *137*, 501.
[45] O. Poncelet, L. Hubert-Pfalzgraf, J. C. Daran, *Polyhedron* **1990**, *9*, 1305.
[46] M. Jupa, G. Kickelbick, U. Schubert, *Eur. J. Inorg. Chem.* **2004**, 1835.
[47] M. A. Subhana, H. Nakatab, T. Suzukia, J. H. Choia, S. Kaizaki, *J. Lumin.* **2003**, *101*, 307.
[48] M. Jupa, G. Kickelbick, U. Schubert, *Eur. J. Inorg. Chem.* **2004**, 1835.
[49] L. G. Hubert-Pfalzgraf, N. Miele-Pajot, R. Papiernik, J. Vaissermann, *J. Chem. Soc. Dalton Trans.* **1999**, 4127.

Received: May 27, 2009
Published online: October 6, 2009

